Superfluid phases of ^{3}He in nanoscale channels

J. J. Wiman and J. A. Sauls

Phys. Rev. B **92**, 144515 — Published 30 October 2015

DOI: 10.1103/PhysRevB.92.144515

Superfluid phases of ^{3}He in nano-scale channels

J. J. Wiman and J. A. Sauls
Department of Physics and Astronomy, Northwestern University, Evanston, Illinois 60208
(Dated: October 12, 2015)

Confinement of superfluid ^{3}He on length scales comparable to the radial size of the p-wave Cooper pairs can greatly alter the phase diagram by stabilizing broken symmetry phases not observed in bulk ^{3}He. We consider superfluid ^{3}He confined within long cylindrical channels of radius 100 nm, and report new theoretical predictions for the equilibrium superfluid phases under strong confinement. The results are based on the strong-coupling formulation of Ginzburg-Landau theory with precise numerical minimization of the free energy functional to identify the equilibrium phases and their regions of stability. We introduce an extension of the standard GL strong-coupling theory that accurately accounts for the phase diagram at high pressures, including the tri-crital point and $T_{AB}(p)$ line defining the region of stability for the bulk A-phase. We also introduce tuneable boundary conditions that allow us to explore boundary scattering ranging from maximal to minimal pairbreaking, and report results for the phase diagram as a function of pressure, temperature, and boundary conditions. Four stable phases are found: a polar phase stable in the vicinity of T_c, a strongly anisotropic, cylindrical analog of the bulk B phase stable at sufficiently low temperatures, and two chiral A-like phases with distinctly different orbital symmetry, one of which spontaneously breaks rotation symmetry about the axis of the cylindrical channel. The relative stability of these phases depends sensitively on pressure and the degree of pairbreaking by boundary scattering. The broken symmetries exhibited by these phases give rise to distinct signatures in transverse NMR resonance spectroscopy. We present theoretical results for the transverse NMR frequency shifts as functions of temperature, the *rf* pulse tipping angle and the static NMR field orientation.

I. INTRODUCTION

Superfluid ^{3}He is a spin-triplet, p-wave Fermi superfluid, where not only is $\mathsf{U}(1)_N$ symmetry spontaneously broken but also spin and orbital rotation symmetries $\mathsf{SO}(3)_S \times \mathsf{SO}(3)_L$. There are a myriad of ways to break these symmetries, leading to many potential superfluid phases. In bulk ^{3}He, in the absence of a magnetic field, only two stable phases are observed: the A phase and the B phase. However, other phases may be stabilized by introducing symmetry breaking terms, such as a magnetic field, impurities, or boundaries, which couple to the spin and orbital degrees of freedom of the Cooper pairs. In particular, confining surfaces suppress Cooper pairs with relative momentum normal to the surface, which leads to a long-range orienting effect on the orbital order parameter.[1] When confined within distances comparable to the Cooper pair coherence length, $\xi_0 \approx 160 - 770\,\text{Å}$ depending on pressure, the influence of the confining surfaces can stabilize phases much different than those of bulk superfluid ^{3}He.

Advances in nanoscale fabrication techniques,[2] as well as the production of porous materials with interesting structure on the coherence length scale,[3,4] have made studies of the effects of strong confinement on broken symmetry phases of topological quantum materials feasible, and have brought a surge of research on the effects of confinement on superfluid ^{3}He.[5–9] One of the simplest confining geometries is the pore, a long, small radius cylinder. The pore has long been of theoretical interest due to the number of different A-phase textures that might be stabilized,[10] as well the effects of radial confinement on the superfluid phase diagram.[11–13] Nuclear magnetic resonance (NMR) experiments in $2\,\mu$m diameter pores have observed A-like textures,[14,15] but have had difficulty definitively identifying the textures present.[16] New fabrication techniques for porous membranes[17] have made available pores with diameters below $1\,\mu$m, which, coupled with an array of new experimental techniques,[2,18–20] open new windows into superfluid ^{3}He under strong confinement.

In this paper we consider an infinitely long cylindrical pore of radius $R = 100\,\text{nm}$, and we study the equilibrium phases in Ginzburg-Landau (GL) theory and identify their signatures in nonlinear NMR spectroscopy. By incorporating pressure dependent strong-coupling corrections to the GL material coefficients, and a tuneable pairbreaking boundary condition, we obtain phase diagrams as functions of temperature, pressure, and surface condition. Finally, we derive expressions for the transverse NMR frequency shifts of the equilibrium phases of ^{3}He confined in the pore as functions of *rf* pulse driven tipping angle, and show how they vary with order parameter symmetry and orientation of the static magnetic field.

II. GINZBURG-LANDAU THEORY

We use Ginzburg-Landau theory calculations of the superfluid ^{3}He order parameter and free energy to determine the stable phases present in the pore. The order parameter for superfluid ^{3}He, given by the manifold of spin-triplet, p-wave BCS pairing states, may be represented by the 2×2 gap matrix,

$$\hat{\Delta}(\hat{p}) = \sum_{\alpha i} A_{\alpha i}\,(i\sigma_\alpha\sigma_y)\,\hat{p}_i\,, \tag{1}$$

which depends on the direction of the relative momentum $\hat{p}$ of the Cooper pairs, and is parameterized by the 3×3 complex matrix order parameter A. The matrix A transforms as a vector under spin rotations, and separately as a vector under orbital rotations. In cylindrical coordinates $A_{\alpha i}$ can be represented as

$$A = \begin{pmatrix} A_{rr} & A_{r\phi} & A_{rz} \\ A_{\phi r} & A_{\phi\phi} & A_{\phi z} \\ A_{zr} & A_{z\phi} & A_{zz} \end{pmatrix} , \tag{2}$$

where we have chosen aligned spin and orbital coordinate axes.

The presence of boundaries reduces the possible residual orbital symmetries of the superfluid phases to be elements of the point group of the confining cylindrical geometry. However, this reduction in symmetry is due to interactions atomically close to the boundary surface; away from the surface, the ^{3}He particle-particle interactions are still invariant under the maximal symmetry group of bulk ^{3}He. Thus, the Ginzburg-Landau free energy functional is given by the invariants of the bulk ^{3}He symmetry group,

$$\mathsf{G}_{\rm bulk} = \mathsf{U}(1) \times \mathsf{SO}(3)_{\rm S} \times \mathsf{SO}(3)_{\rm L} \times \mathsf{P} \times \mathsf{T} , \tag{3}$$

which is the product of global gauge rotations, spin rotations, orbital rotations, space inversion, and time-reversal, respectively. The resulting free energy functional is

$$\Omega[A] = \int_V d^3r \, \left(f_{\rm bulk}[A] + f_{\rm grad}[A] \right) . \tag{4}$$

The terms $f_{\rm bulk}$ and $f_{\rm grad}$ are given by

$$\begin{aligned} f_{\rm bulk}[A] = {} & \alpha(T) Tr\left(AA^\dagger\right) + \beta_1 \left|Tr(AA^T)\right|^2 + \beta_2 \left[Tr(AA^\dagger)\right]^2 \\ & + \beta_3 Tr\left[AA^T(AA^T)^*\right] + \beta_4 Tr\left[(AA^\dagger)^2\right] + \beta_5 Tr\left[AA^\dagger(AA^\dagger)^*\right] , \end{aligned} \tag{5}$$

$$\begin{aligned} f_{\rm grad}[A] = {} & K_1 A^*_{\alpha j,k} A_{\alpha j,k} + K_2 A^*_{\alpha j,j} A_{\alpha k,k} + K_3 A^*_{\alpha j,k} A_{\alpha k,j} \\ & + \frac{2}{r} \mathrm{Re}\left\{ K_1 \left(A^*_{rj} A_{\phi j,j} - A^*_{\phi j} A_{rj,\phi} + A^*_{ir} A_{i\phi,\phi} - A^*_{i\phi} A_{ir,\phi} \right) \right. \\ & \qquad + K_2 \left(A^*_{r\phi} A_{\phi j,j} - A^*_{\phi\phi} A_{rj,j} + A^*_{ir} A_{ij,j} \right) \\ & \qquad \left. + K_3 \left(A^*_{rj} A_{\phi\phi,j} - A^*_{\phi j} A_{r\phi,j} + A^*_{ir} A_{i\phi,\phi} - A^*_{i\phi} A_{i\phi,r} \right) \right\} \\ & + \frac{1}{r^2} \left\{ K_1 \left[A^*_{rj} A_{rj} + A^*_{\phi j} A_{\phi j} + A^*_{ir} A_{ir} + A^*_{i\phi} A_{i\phi} + 4\mathrm{Re}(A^*_{r\phi} A_{r\phi} - A^*_{rr} A_{\phi\phi}) \right] \right. \\ & \qquad \left. + (K_2 + K_3) \left[|A_{r\phi}|^2 + |A_{\phi\phi}|^2 + A^*_{ir} A_{ir} + 2\mathrm{Re}(A^*_{r\phi} A_{\phi r} - A^*_{rr} A_{\phi\phi}) \right] \right\} , \end{aligned} \tag{6}$$

where $A^\dagger$ (A^T) is the adjoint (transpose) of A, and

$$A_{\alpha i,j} \equiv \left\{ \frac{\partial A_{\alpha i}}{\partial r} , \, \frac{1}{r} \frac{\partial A_{\alpha i}}{\partial \phi} , \, \frac{\partial A_{\alpha i}}{\partial z} \right\}_j . \tag{7}$$

The term $f_{\rm bulk}$ holds for any orthogonal coordinate system, whereas $f_{\rm grad}$ is coordinate specific and given in the form derived by Buchholtz and Fetter.[21] In the weak-coupling BCS limit the material parameters,

$$\alpha^{\rm wc}(T) = \frac{1}{3} N(0) (T/T_c - 1) , \tag{8}$$

$$2\beta_1^{\rm wc} = -\beta_2^{\rm wc} = -\beta_3^{\rm wc} = -\beta_4^{\rm wc} = \beta_5^{\rm wc} , \tag{9}$$

$$\beta_1^{\rm wc} = -\frac{N(0)}{(\pi k_{\rm B} T_c)^2} \left\{ \frac{1}{30} \left[\frac{7}{8} \zeta(3) \right] \right\} , \tag{10}$$

$$K_1^{\rm wc} = K_2^{\rm wc} = K_3^{\rm wc} = \frac{7\zeta(3)}{60} N(0) \, \xi_0^2 , \tag{11}$$

are determined by the normal-state (single-spin) density of states at the Fermi energy, $N(0)$, the bulk superfluid transition temperature, T_c, and the Fermi velocity, v_f. Note that $\xi_0 = \hbar v_f / 2\pi k_B T_c$ is the Cooper pair correlation length, which varies from $\xi_0 \simeq 770\,$Å at $p = 0\,$bar to $\xi_0 \simeq 160\,$Å at $p = 34\,$bar. The equilibrium order parameter is obtained from minimization of the free energy functional by solving the Euler-Lagrange equations obtained from the functional gradient $\delta\Omega[A]/\delta A^\dagger = 0$.

A. Strong-coupling Corrections

The weak-coupling GL material parameters are derived from the leading order contribution to the full Luttinger-Ward free energy functional as an expansion in the small parameter T/T_F, where $T_F = E_F/k_B \approx 1\,$K is the Fermi temperature. In particular, $\Omega^{\rm wc} \sim (T_c/T_F)^2 E_N$, where E_N is the ground-state energy of the normal Fermi liquid. The next-to-leading corrections to the weak-coupling GL functional enter as corrections to the fourth-order weak-coupling material coefficients. These corrections are of order $\Delta\beta_i^{\rm sc} \approx \beta_i^{\rm wc}(T/T_F)\langle w_i|A|^2\rangle$, where $\langle w_i|A|^2\rangle$ is a

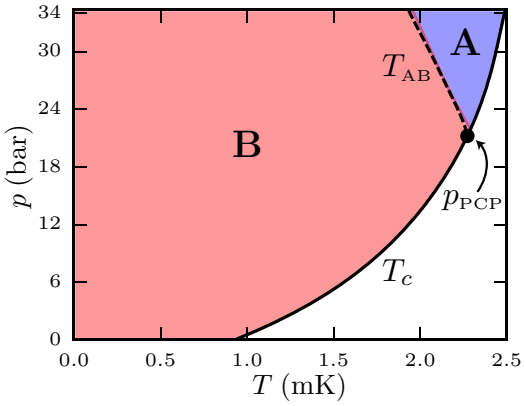

FIG. 1: The bulk phase diagram showing the regions of stability of the A (blue) and B (red) phases using the experimental βs with linear T scaling. The dashed line is the experimental A-B transition line terminating at the experimental PCP point.

weighted average of the square of the scattering amplitude for binary collisions between quasiparticles on the Fermi surface.[22] At high pressures, scattering due to ferromagnetic spin fluctuations largely compensates the small parameter T/T_F, resulting in substantial strong-coupling corrections.[23]

While the $\Delta\beta_i^{\rm sc}$'s may be calculated theoretically through a model of the quasiparticle scattering amplitude[23], the most current determinations come from comparison with experiment.[24] In the main analysis presented here we use the set of $\{\beta_i\}$ reported by Choi et al.[24] These β-parameters reproduce the heat capacity jumps for the A and B transitions, which is essential when considering the energetics of A and B-like phases. In particular, the A phase correctly appears as a stable phase above the polycritical point $p_{\rm PCP} = 21.22\,$bar; however, in fourth-order GL theory it is the only stable phase at all temperatures above the PCP, i.e. the standard fourth-order GL theory fails to account for the A-B transition line, $T_{\rm AB}(p)$. The missing transition line is traced to the omission of the temperature dependence of the fourth-order β parameters in the neighborhood of a tri-critical point. In particular, the tri-critical point is defined by the intersection of the second-order transition line given by $\alpha(T_c, p) = 0$, and the first-order boundary line separating the A- and B-phases given by $\Delta\beta_{AB}(T_{\rm AB}, p) \equiv \beta_A - \beta_B = 0$. Note that $\beta_A \equiv \beta_{245}$ and $\beta_B \equiv \beta_{12} + \frac{1}{3}\beta_{345}$ where we use the stanadard notation, $\beta_{ijk\ldots} = \beta_i + \beta_j + \beta_k + \ldots$.[22] At the PCP we have $T_{\rm AB}(p_{\rm PCP}) = T_c(p_{\rm PCP})$. But, for $p > p_{\rm PCP}$ the lines separate and we must retain both the temperature and pressure dependences of $\Delta\beta_{AB}(T,p)$ to account for $T_{\rm AB}(p)$ in the vicinity of $p_{\rm PCP}$. This is achieved with remarkable success by making a single correction to the standard treatment of strong-coupling corrections within GL theory. Near T_c the leading-order strong-coupling corrections to the weak-coupling β parameters scale as $\Delta\beta_i^{\rm sc} \sim (T/T_F)|\beta_1^{\rm wc}|$, where the linear scaling with T/T_F originates from the limited phase space for binary collisions of quasiparticles at low temperatures. Resolving the degeneracy between the A- and B-phases near $p_{\rm PCP}$ is achieved by retaining the linear T dependence of the strong-coupling corrections to the β parameters. Thus, we separate the β parameters determined at p and $T_c(p)$ into the weak- and strong-coupling parts using Eq. 9, and then scale the strong-coupling corrections, $\Delta\beta_i^{\rm sc}$, determined at $T_c(p)$ in Ref. 24 and listed in Tables I and II of the Appendix,

$$\beta_i(T,p) = \beta_i^{\rm wc}(p, T_c(p)) + \frac{T}{T_c}\Delta\beta_i^{\rm sc}(p)\,, \qquad (12)$$

$$\text{with} \quad \Delta\beta_i^{\rm sc}(p) = \beta_i(p, T_c(p)) - \beta_i^{\rm wc}(p, T_c(p))\,. \qquad (13)$$

The resulting bulk phase diagram predicted by these GL parameters accounts remarkably well for the experimental A-B transition line, $T_{\rm AB}(p)$, as shown in Fig. 1, as well as the heat capacity jumps and the PCP along $T_c(p)$. This result for the bulk phase diagram gives us confidence in our predictions for the equilibrium phases of confined ^{3}He based on strong-coupling GL theory. The main analysis and predictions for inhomogeneous phases of superfluid ^{3}He reported here are based on the strong-coupling material parameters from Ref. 24 combined with the known pressure-dependent material parameters, v_f, T_c, and ξ_0 as listed in Table I in the Appendix, and the temperature scaling in Eq. 12 that accounts for the relative reduction of strong-coupling effects below T_c.

B. Sauls-Serene β parameters

The individual $\Delta\beta_i^{\rm sc}$ parameters reported by Choi et al.[24] differ from those calculated from leading order strong-coupling theory, or those obtained from the analysis of different experiments, even though the different sets predict the same bulk phase diagram.

As a test of the sensitivity of our GL predictions for new phases in confined geometries to the details of the model for the strong-coupling GL β parameters we also calculated the phase diagram based on the $\{\beta_i\}$ predicted by the leading order strong-coupling theory.[22,23] The theoretical values for the strong-coupling β parameters are determined by angular averages of the normal-state quasiparticle scattering rate. The analysis of Sauls and Serene is based on a quasiparticle scattering amplitude that accounts for the effective mass, the ferromagnetic enhancement of the spin susceptibility and the normal-state transport coefficients.[23] The Sauls-Serene β-parameters, summarized in Tables III and IV, reproduce the relative stability of the bulk A and B phases, albeit with an elevated polycrital pressure of $p_{\rm PCP} \simeq 28\,$bar.

The results for the phase diagram with these two different sets of $\Delta\beta_i^{\rm sc}$, discussed in Sec. IV, give robust predictions for the relative stabilty of new inhomogeneous phases of ^{3}He confined in cylindrical pores.

C. Boundary Conditions

For planar surfaces there are two limiting boundary conditions applicable within GL theory: maximal pairbreaking, resulting from retro-reflection of quasiparticles,[27] and minimal pairbreaking, resulting from specular reflection.[1] If we use cartesian coordinates and take the surface to lie along the $x-y$ plane with ^{3}He occupying $z > 0$, then maximal pairbreaking is defined by the condition

$$A_{\alpha i}\big|_{z=0} = 0 \;\forall i \in \{x, y, z\}\,, \tag{14}$$

while minimal pairbreaking is defined by the conditions

$$\begin{aligned} A_{\alpha z}\big|_{z=0} &= 0\,, \\ \nabla_z A_{\alpha x}\big|_{z=0} &= \nabla_z A_{\alpha y}\big|_{z=0} = 0\,. \end{aligned} \tag{15}$$

In a cylindrical pore, additional care needs to be given to the boundary conditions due to the presence of curvature on scales comparable to the coherence length. While the boundary condition for maximal pairbreaking is not modified, the curved surface of the pore modifies the minimal pairbreaking boundary condition for the azimuthal orbital components of the order parameter, $A_{\alpha\phi}$. Fetter and Buchholtz proposed a minimal pairbreaking boundary condition in GL theory based on the Euler-Lagrange boundary term of the GL equations with a cylindrical surface,[21]

$$\left.\frac{\partial A_{\alpha z}}{\partial r}\right|_{r=R} = 0\,, \quad A_{\alpha r}|_{r=R} = 0\,, \tag{16}$$

$$\left.\frac{\partial A_{\alpha\phi}}{\partial r}\right|_{r=R} = \frac{1}{R} A_{\alpha\phi}|_{r=R}\,. \tag{17}$$

We introduce an extension of these boundary conditions which interpolates between the two extremes of minimal and maximal pairbreaking. The extension is based on Ambegaokar, de Gennes, and Rainer's (AdGR) analysis[1] of the effects of diffuse scattering by an atomically rough surface on the transverse components of the p-wave orbital order parameter. AdGR showed that diffuse scattering leads to a boundary condition in which the components that are transverse to the average normal direction of the surface are finite, but extrapolate linearly to zero past the boundary at a distance $b_T = 0.54\xi_0$. This idea can be turned into a more general boundary condition for GL theory in a cylindrical geometry as

$$\begin{aligned} A_{\alpha r}|_{r=R} &= 0\,, \\ \left.\frac{\partial A_{\alpha z}}{\partial r}\right|_{r=R} &= -\frac{1}{b_T} A_{\alpha z}|_{r=R}\,, \\ \left.\frac{\partial A_{\alpha\phi}}{\partial r}\right|_{r=R} &= \left(\frac{1}{R} - \frac{1}{b_T}\right) A_{\alpha\phi}|_{r=R}\,. \end{aligned} \tag{18}$$

where $b_T' \equiv b_T/\xi_0$ can be treated as a parameter that varies between the maximal pairbreaking ($b_T' \to 0$) and minimal pairbreaking ($b_T' \to \infty$) limits. This generalized "AdGR" boundary condition provides a useful extension of the typical Ginzburg-Landau boundary conditions.

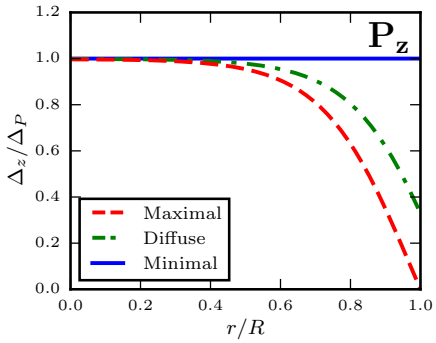

FIG. 2: Order parameter amplitudes for the $\mathrm{P_z}$ phase as a function of r at $p = 26\,\mathrm{bar}$ and $T = 0.5\,T_c$ for retro-reflection (maximal pair-breaking), diffuse ($b_T' = 0.54$), and specular (minimal pair-breaking) boundary conditions. Values are scaled by the unconfined polar phase amplitude $\Delta_P^2 = |\alpha(T)|/2\beta_{12345}$. For minimal pairbreaking boundary conditions the $\mathrm{P_z}$ phase is spatially homogeneous within the pore.

III. SUPERFLUID PHASES

The pore geometry reduces the maximal symmetry group for confined ^{3}He to

$$\mathsf{G} = \mathsf{U}(1)_\mathrm{N} \times \mathsf{SO}(3)_\mathrm{S} \times \mathsf{D}_{\infty\mathrm{h}} \times \mathsf{T} \tag{19}$$

where $\mathsf{D}_{\infty\mathrm{h}}$ is the point group of the pore and is obtained from the point group of the circle, $\mathsf{C}_{\infty\mathrm{v}} = \mathsf{SO}(2) \times \{\mathrm{e}, \pi_{zx}\}$, by $\mathsf{D}_{\infty\mathrm{h}} = \mathsf{C}_{\infty\mathrm{v}} \times \{\mathrm{e}, \pi_{xy}\}$, where π_{xy} is a reflection through the $x-y$ plane. By numerically minimizing the GL free energy with respect to all order parameter components we identify four equilibrium superfluid phases for the 200 nm pore. In these calculations we assume the phases are translationally invariant along the z axis.[28]

A. Polar ($\mathrm{P_z}$) Phase

Radial confinement in a cylindrical pore leads to the stability of the one-dimensional polar ($\mathrm{P_z}$) phase below $T_{c_1} \le T_c$, where T_{c_1} is the transition temperature from the normal state. The $\mathrm{P_z}$ phase is a time-reversal invariant equal-spin pairing (ESP) phase with an order parameter of form

$$A_{\alpha i} = \Delta_z(r)\, \hat{d}_\alpha\, \hat{z}_i\,, \tag{20}$$

with radial profile shown in Fig. 2. The $\mathrm{P_z}$ order parameter becomes spatially homogeneous with $T_{c_1} \to T_c$ in the limit of specular scattering, and will be the first superfluid phase upon cooling from the normal state, except for the exceptional case of perfect specular reflection and perfect cylindrical cross-section (see Sec. III C). The residual symmetry group of the $\mathrm{P_z}$ phase is $\mathsf{H} = \mathsf{SO}(2)_{\mathrm{S_d}} \times \mathsf{Z}_2^{\mathrm{spin}} \times \mathsf{D}_{\infty\mathrm{h}}^{\mathrm{L},\pi} \times \mathsf{T}$, where $\mathsf{D}_{\infty\mathrm{h}}^{\mathrm{L},\pi} \equiv \mathsf{C}_{\infty\mathrm{v}} \times \{\mathrm{e}, e^{i\pi}\pi_{xy}\}$. Thus, the $\mathrm{P_z}$ phase breaks spin rotational symmetry but retains the full orbital point group,

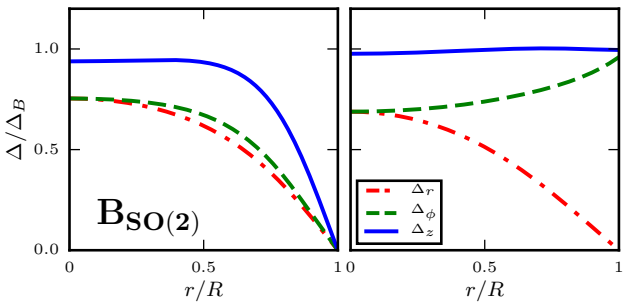

FIG. 3: Order parameter amplitudes for the $\mathrm{B}_{\mathbf{SO(2)}}$ phase as a function of r at $p = 26\,\mathrm{bar}$ and $T = 0.5\,T_c$. The left figure depicts maximal pairbreaking ($b'_T = 0$) while the right shows minimal pairbreaking ($b'_T = \infty$). Values are scaled by the bulk B phase order parameter, $\Delta_B^2 = |\alpha(T)|/6(\beta_{12}+1/3\beta_{345})$.

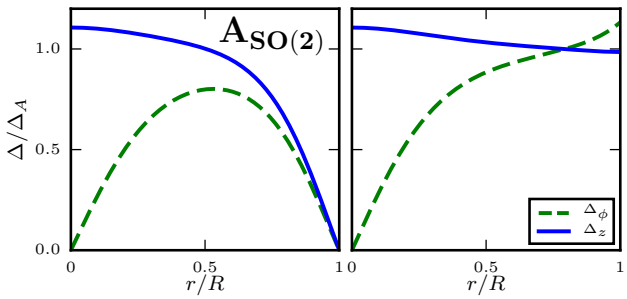

FIG. 4: Order parameter amplitudes for the $\mathrm{A}_{\mathbf{SO(2)}}$ phase as a function of r at $p = 26\,\mathrm{bar}$ and $T = 0.5\,T_c$. The left figure depicts maximal pairbreaking while the right shows minimal pairbreaking. Values are scaled by the bulk A phase order parameter, $\Delta_A^2 = |\alpha(T)|/4\beta_{245}$.

$\mathsf{D}_{\infty\mathrm{h}}$, by combining it with an element of the gauge group. Since the radius $R = 100\,\mathrm{nm}$ of the pore is much less than the dipole coherence length, $\xi_\mathrm{D} \approx 10 - 20\,\mu\mathrm{m}$, the spin quantization axis, $\hat{d}$, for the ESP state is to high accuracy uniform in space. All transitions to and from the $\mathrm{P}_\mathbf{z}$ phase that we find are second order.

B. $\mathrm{B}_{\mathbf{SO(2)}}$ Phase

The $\mathrm{B}_{\mathbf{SO(2)}}$ phase is the analogue to the bulk B phase for the cylindrical pore geometry, and is stabilized at low temperatures and preferentially favored by strong pair-breaking on the boundary. The residual symmetry of the $\mathrm{B}_{\mathbf{SO(2)}}$ phase is $\mathsf{H} = \mathsf{D}_{\infty\mathrm{h}}^{\mathrm{L+S}} \times \mathsf{T}$, joint spin and orbital $\mathsf{D}_{\infty\mathrm{h}}$ transformations combined with time-reversal. The order parameter is represented as

$$A_{\alpha i} = \Delta_r(r)\hat{r}_\alpha\hat{r}_i + \Delta_\phi(r)\hat{\phi}_\alpha\hat{\phi}_i + \Delta_z(r)\hat{z}_\alpha\hat{z}_i\,, \qquad (21)$$

with the radial profiles shown in Fig. 3.

C. $\mathrm{A}_{\mathbf{SO(2)}}$ Phase

In addition to the $\mathrm{P}_\mathbf{z}$ and $\mathrm{B}_{\mathbf{SO(2)}}$ phases, we find two stable chiral A-like phases. The higher symmetry $\mathrm{A}_{\mathbf{SO(2)}}$ phase, reminiscent of the "radial disgyration texture" of bulk ^{3}He-A, is favored by weak pair-breaking on the boundary. The residual symmetry group of the $\mathrm{A}_{\mathbf{SO(2)}}$ phase is $\mathsf{H} = \mathsf{SO}(2)_{\mathrm{S_d}} \times \mathsf{Z}_2^{\mathrm{spin}} \times \mathsf{D}_{\infty\mathrm{h}}^{\mathrm{L,T}}$, where $\mathsf{D}_{\infty\mathrm{h}}^{\mathrm{L,T}} \equiv \mathsf{SO}(2) \times \{\mathrm{e},\, \mathrm{t}\pi_{zx}\} \times \{\mathrm{e},\, e^{i\pi}\mathrm{t}\pi_{xy}\}$ and t is time reversal. The order parameter takes the form

$$A_{\alpha i} = \hat{d}_\alpha[\Delta_z(r)\hat{z}_i + i\,\Delta_\phi(r)\hat{\phi}_i] \qquad (22)$$

which is transverse to the pore boundary with radial profiles shown in Fig. 4. The chiral vector,

$$\vec{l} = -\Delta_z(r)\Delta_\phi(r)\,\hat{r}\,, \qquad (23)$$

shown in Fig. 5, is radial except at the origin where $\vec{l}$ vanishes; the gradient terms in the GL functional require

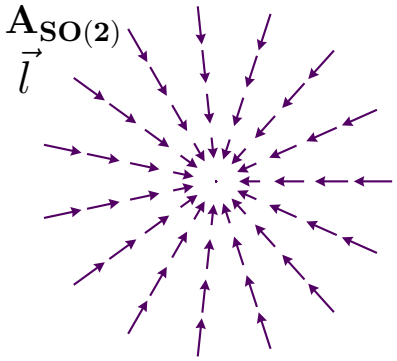

FIG. 5: Chiral axis $\hat{l}$ for the $\mathrm{A}_{\mathbf{SO(2)}}$ phase at $p = 26\,\mathrm{bar}$, $T = 0.5\,T_c$, and minimal pairbreaking boundaries. Arrow lengths are scaled by $|\Delta_\phi|$.

$\Delta_\phi = 0$, yielding a polar order parameter at the core of the cylindrical pore. The resulting chiral field is analogous to a radial disgyration - a topological line defect of bulk ^{3}He-A. This form for $\vec{l}$ results in a zero average of $\vec{l}(r)$ over the cylindrical pore, which leads to distinctly different NMR frequency shift for the $\mathrm{A}_{\mathbf{SO(2)}}$ phase as compared with a chiral state with a non-vanishing average chiral axis, $\langle\vec{l}(\vec{r})\rangle \neq 0$, as discussed in Sec. V. For the specular boundary condition proposed in Ref. 21 (Eq. 18 with $b'_T \to \infty$), the $\mathrm{A}_{\mathbf{SO(2)}}$ phase entirely supplants the $\mathrm{P}_\mathbf{z}$ phase, and onsets at the bulk transition temperature T_c, despite being spatially inhomogeneous.

D. $\mathrm{A}_{\mathbf{C_2}}$ Phase

A lower symmetry A-like phase, denoted as $\mathrm{A}_{\mathbf{C_2}}$, is an inhomogenous version of the the circular disgyration, or Pan Am texture.[10,14] This phase spontaneously breaks continuous $\mathsf{SO}(2)_L$ symmetry of the cylinder and, unlike

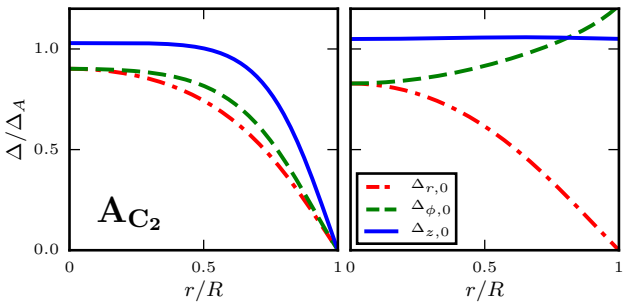

FIG. 6: Dominant order parameter amplitudes for the $\mathrm{A}_{\mathbf{C_2}}$ phase at $p = 26\,\mathrm{bar}$ and $T = 0.5\,T_c$. The left figure depicts maximal pairbreaking while the right shows minimal pairbreaking. Values are scaled by the bulk A phase amplitude $\Delta_A^2 = |\alpha(T)|/4\beta_{245}$.

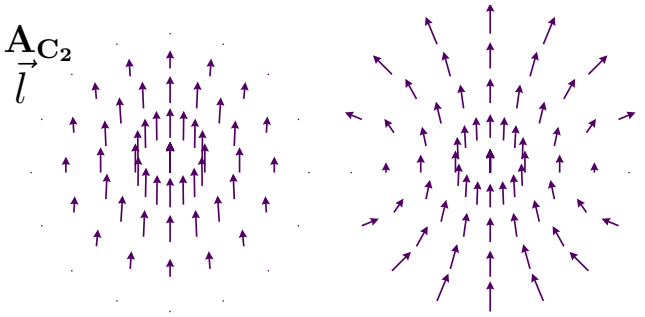

FIG. 7: Chiral axis $\hat{l}$ for the $\mathrm{A}_{\mathbf{C_2}}$ phase at $p = 26\,\mathrm{bar}$ and $T = 0.5\,T_c$. (Left) Maximal pairbreaking boundaries result in a nearly uniform $\hat{l}$ direction. (Right) Minimal pairbreaking, on the other hand, gives the characteristic "Pan Am" configuration. Arrow lengths are scaled by $(\Delta_r^2 + \Delta_\phi^2)^{1/2}$.

the $\mathrm{A}_{\mathbf{SO(2)}}$ phase, has a finite value for the spatially averaged chiral axis, $\langle\vec{l}\rangle \neq 0$, that may point in any direction in the $x-y$ plane. For convenience we take $\langle\vec{l}\rangle \parallel \hat{y}$, with an order parameter of the form

$$A_{\alpha i} = \hat{d}_\alpha[\Delta_z(r,\phi)\hat{z}_i + i\,\Delta_r(r,\phi)\hat{r}_i + i\,\Delta_\phi(r,\phi)\hat{\phi}_i]\,. \quad (24)$$

The residual symmetry group is then $\mathsf{H} = \mathsf{SO}(2)_{\mathrm{S_d}} \times \mathsf{Z}_2^{\mathrm{spin}} \times \mathsf{D}_{2\mathrm{h}}^{\mathrm{L,T}}$, where $\mathsf{D}_{2\mathrm{h}}^{\mathrm{L,T}} \equiv \{\mathrm{e}, \mathrm{t}c_2, \pi_{zx}, \mathrm{t}\pi_{zy}\} \times \{\mathrm{e}, e^{i\pi}\mathrm{t}\pi_{xy}\}$. The $\mathrm{A}_{\mathbf{C_2}}$ phase has a pair of disgyrations on the boundary along an axis perpendicular to $\hat{z}$ and $\langle\vec{l}\rangle$, as can be seen for the case of minimal pairbreaking in Fig. 7. The $\mathrm{A}_{\mathbf{C_2}}$ phase is energetically favorable relative to the $\mathrm{A}_{\mathbf{SO(2)}}$ phase for strong pairbreaking on the boundary. In this case the boundary effectively "censors" the energy cost of the $\mathrm{A}_{\mathbf{C_2}}$ disgyrations. The suppression of the disgyrations is evident in Fig. 7.

The $\mathrm{A}_{\mathbf{C_2}}$ phase is the only phase we find with broken axial symmetry, and thus explicit ϕ dependence. It is convenient to expand its amplitudes in terms of sines and cosines that respect symmetry,

$$A_{\alpha i} = \hat{d}_\alpha \sum_{j=0}^{\infty} \Big\{ i\,\Delta_{r,j}(r)\cos[(2j+1)\phi]\,\hat{r}_i - i\,\Delta_{\phi,j}(r)\sin[(2j+1)\phi]\,\hat{\phi}_i + \Delta_{z,j}(r)\cos(2j\phi)\,\hat{z}_i \Big\}\,. \quad (25)$$

Numerical solutions to the GL equations converge rapidly as a function of the number of azimuthal harmonics, which greatly simplifies the numerical minimization compared to allowing for an arbitrary ϕ dependence.

IV. PHASE DIAGRAM

The phase diagram for superfluid ^{3}He confined within a pore is strongly dependent upon the boundary conditions. We first fix $R = 100\,\mathrm{nm}$ and consider the phase diagram for four different values of b_T', ranging from minimal to maximal pairbreaking as shown in Figures 8 and 9. For strong pairbreaking (Fig. 8) the phase diagram is dominated by the $\mathrm{B}_{\mathbf{SO(2)}}$, $\mathrm{A}_{\mathbf{C_2}}$, and $\mathrm{P}_{\mathbf{z}}$ phases. In this regime, our phase diagram differs from previous calculations[11,13] due to the appearance of the $\mathrm{A}_{\mathbf{C_2}}$ phase, which for strong pairbreaking has a lower free energy than that of the $\mathrm{A}_{\mathbf{SO(2)}}$ phase. As pairbreaking decreases on the boundary, the $\mathrm{A}_{\mathbf{SO(2)}}$ phase appears at high pressure, with a tri-critical point separating the $\mathrm{B}_{\mathbf{SO(2)}}$, $\mathrm{A}_{\mathbf{SO(2)}}$ and $\mathrm{A}_{\mathbf{C_2}}$ phases. The $\mathrm{A}_{\mathbf{SO(2)}}$ phase occupies most of the superfluid phase diagram for minimal pairbreaking boundaries. It must be noted, however, that any deviation from the perfect specular condition $b_T' = \infty$ will suppress $A_{\alpha\phi}$ at the boundary near T_c, and thus the $\mathrm{P}_{\mathbf{z}}$ phase should always be expected to be the highest temperature superfluid phase observed experimentally.

We also consider the influence of the pore radius, R, on stability of the various phases. Fig. 10 shows the phase diagram of stable phases in a cylindrical channel as a function of the pore radius relative to the coherence length, R/ξ_0. For a range of sufficiently small R/ξ_0 only the $\mathrm{P}_{\mathbf{z}}$ phase is stable; the $\mathrm{B}_{\mathbf{SO(2)}}$, $\mathrm{A}_{\mathbf{C_2}}$, and $\mathrm{A}_{\mathbf{SO(2)}}$ phases enter the diagram with increasing R. The $\mathrm{A}_{\mathbf{SO(2)}}$ phase is favored over the $\mathrm{A}_{\mathbf{C_2}}$ phase for large radii; however, the relative stability of these two chiral phases is sensitive to boundary scattering, i.e. b_T', as shown in Figs. 8 and 9. For larger radii of order the dipole coherence length, $R \approx \xi_D \approx 10\,\mu\mathrm{m}$, the spin quantization axis, $\hat{d}$, for the $\mathrm{A}_{\mathbf{C_2}}$ and $\mathrm{A}_{\mathbf{SO(2)}}$ phases is no longer constrained to be spatially uniform, and for $R \gg \xi_D$ these phases become "dipole-locked" with $\hat{d} \parallel \hat{l}$.[21]

We also tested the robustness of our predictions for the phase diagram against a different set of strong-coupling β parameters, specifically the Sauls-Serene set of $\Delta\beta_i^{\mathrm{sc}}$ calculated on the basis of leading order strong-coupling theory[22] based on a quasiparticle scattering amplitude that accounts for both the normal-state effective mass,

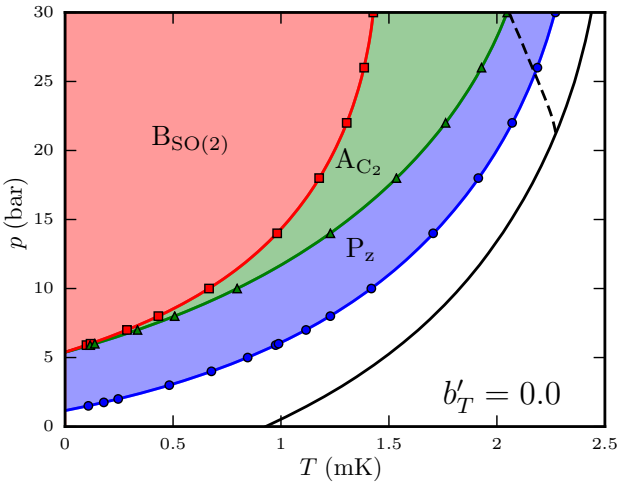

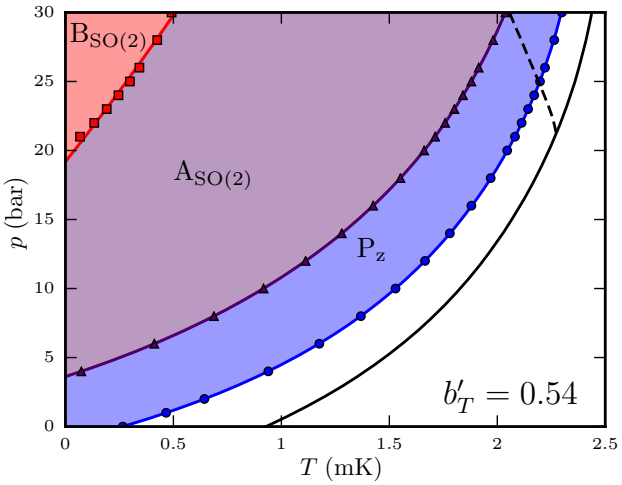

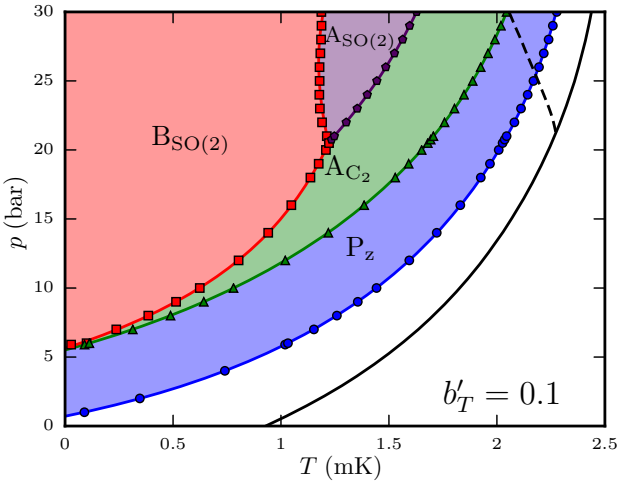

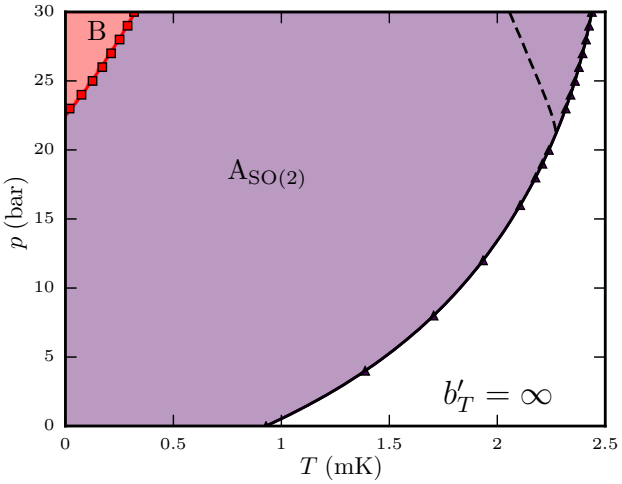

FIG. 8: Phase diagrams for $b'_T = 0$ (maximal pairbreaking) and $b'_T = 0.1$. The $\mathrm{A_{SO(2)}}$ phase does not appear at all for maximal pairbreaking; as pairbreaking at the boundary is relaxed it is stabilized at high pressure and displaces the $\mathrm{B_{SO(2)}}$ and $\mathrm{A_{C_2}}$ phases.

FIG. 9: Phase diagrams for $b'_T = 0.54$ and $b'_T = \infty$ (minimal pairbreaking). As pairbreaking decreases, the $\mathrm{A_{C_2}}$ phase is suppressed completely and the stable range of the $\mathrm{B_{SO(2)}}$ phase is decreased significantly. For minimal pairbreaking the $\mathrm{A_{SO(2)}}$ phase onsets at $T = T_c$ with the $\mathrm{P_z}$ phase absent.

ferromagnetic enhancement of the spin susceptibility and transport coefficients.[23] These β parameters account for the relative stability of the bulk A- and B-phases, but have distinctly different predictions for the pressure dependences of the strong-coupling corrections: $\Delta\beta_i^{\rm sc}$. The key result is that the structure of the phase diagram is unchanged with a different set of strong-coupling β parameters, i.e. the relative stability of the $\mathrm{P_z}$, $\mathrm{B_{SO(2)}}$, $\mathrm{A_{C_2}}$, and $\mathrm{A_{SO(2)}}$ phases is unchanged between the two sets of strong-coupling β parameters. This is shown in Fig. 10.

V. NMR SIGNATURES

The superfluid phases obtained for the narrow pore neglect the nuclear magnetic dipole energy. This is an execellent approximation since the nuclear dipole-dipole interaction energy for dipoles separated by the mean interatomic spacing a is very small compared to the pairing energy scale, $\frac{1}{a^3}(\gamma\hbar/2)^2 \approx 10^{-4}\,\mathrm{mK} \ll T_c \approx \mathrm{mK}$. Nevertheless, the dipole energy gives rise to two important effects - (i) it partially resolves relative spin- orbital degeneracy of the equilibrium states, and (ii) it generates a dynamical torque from the Cooper pairs acting on the total spin when the latter is driven out of equilibrium. The dipolar torque leads to NMR frequency shifts that are characteristic signatures of the broken symmetry phases. In the following we report results for the nonlinear NMR frequency shifts that are "fingerprints" of the $\mathrm{P_z}$, $\mathrm{A_{SO(2)}}$, $\mathrm{A_{C_2}}$, and $\mathrm{B_{SO(2)}}$ phases. Our analysis is based on a spatial and temporal averaging of the Leggett equations for the nonlinear spin dynamics of superfluid ^{3}He.

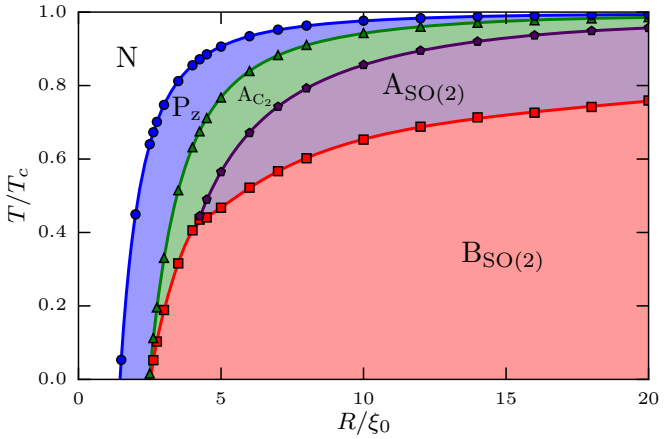

FIG. 10: Temperature-confinement phase diagram for fixed $b'_T = 0.1$, $p = 26$ bar and the β parameters of Ref. 24.

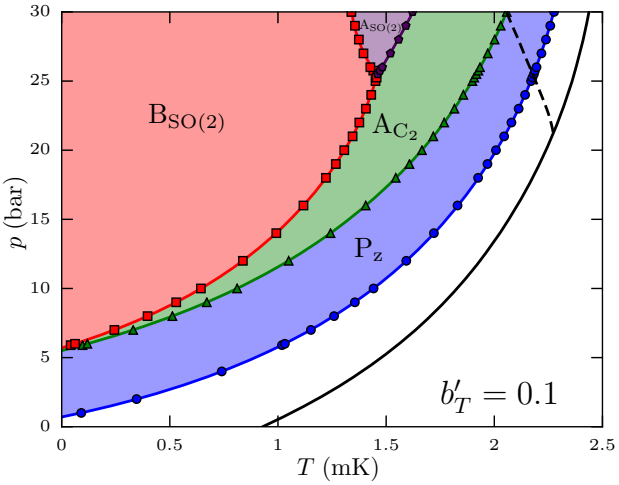

FIG. 11: Phase diagram for $b'_T = 0.1$ using the β parameters of Sauls and Serene.[23] The resulting phase boundaries are largely left unchanged except for the shift upward in pressure of the tricritical point, roughly corresponding to the difference of the Choi et al[24] polycritical point, $p_{\rm PCP} \approx 21$ bar, and the Sauls and Serene polycritical point, $p_{\rm PCP} \approx 28$ bar.

The dipolar interaction breaks relative spin-orbit rotation symmetry, thus reducing the maximal rotational symmetry from $\mathsf{SO}(3)_{\rm S} \times \mathsf{SO}(3)_{\rm L}$ to $\mathsf{SO}(3)_{\rm L+S}$. This is reflected by additional terms in the GL free energy functional, $\Delta\Omega_D = \int_V d^3r\, f_D[A]$, where

$$f_D = g_D \left(|TrA|^2 + TrAA^* \right) \tag{26}$$

is the mean pairing contribution to the nuclear dipolar interaction energy, with $g_D \sim (N(0)\gamma\hbar/2)^2 > 0$. A convenient expression for g_D is $g_{\rm D} = \frac{\chi}{2\gamma^2}\Omega_A^2/\Delta_A^2$, where the A-phase susceptibility, $\chi = \chi_N$, is equal to the normal-state spin susceptibility, Δ_A is the bulk A-phase order parameter, and Ω_A is the corresponding longitudinal resonance frequency. The dipole energy is a weak perturbation that resolves (partially) the relative spin- and orbital degeneracy of the zero-field phases of the cylindrical pore. In particular, for the ESP states of the form $A_{\alpha i} = \hat{d}_\alpha\, \Delta_i(\vec{r})$ the dipolar energy is given by $f_D = g_D\, |\hat{d}\cdot\vec{\Delta}|^2$, which is minimized if $\hat{d}$ *locally* orients perpendicular to the two dominant orbital components. However, spatial variations of the order parameter cost gradient energy. In the case of the orbital components the spatial profiles are already optimized by minimizing the GL functional subject to the boundary conditions of the confining geometry. For the inhomogeneous phases of superfluid ^{3}He in pore of radius $R = 100\,$nm, the spatial variations of the orbital components occur on a length scale that is short compared to the dipole coherence length, $\xi_D \equiv \sqrt{g_D/K_1} \approx 10\,\mu$m. Thus, spatial variations of $\hat{d}$ on such short length scales of the pore geometry cost much more than the dipole energy. As a result $\hat{d}$ "unlocks" from the *local* variations of the orbital order parameter. This allows us to average the orbital components over the cross-section of the cylindrical pore and treat the spin degrees of freedom as spatially uniform on the scale of R. For the non-ESP $\mathrm{B}_{\mathbf{SO(2)}}$ phase the spin structure is described by an orthogonal matrix, $\mathbf{R}[\alpha,\beta,\gamma]$, representing the *relative* rotation of the spin and orbital coordinates.

The orientation of the spin coordinates of the Cooper pairs is also influenced by the nuclear Zeeman energy,

$$\Delta\Omega_Z = g_z \int_V d^3r\, H_\alpha \left(A_{\alpha i} A^*_{\beta i} \right) H_\beta\,, \tag{27}$$

where

$$g_z = \frac{N(0)\gamma^2\hbar^2}{(1+F_0^a)^2}\,\frac{7\zeta(3)}{48\pi^2 T_c^2} > 0\,, \tag{28}$$

is the Zeeman coupling constant in the weak-coupling limit. For ESP states the static NMR field prefers $\hat{d} \perp \vec{H}$.

A. Fast vs. slow spin dynamics

The nuclear dipolar energy generates frequency shifts, $\Delta\omega = \omega - \omega_L$, of the NMR resonace line for superfluid ^{3}He away from the Larmor frequency, $\omega_L = \gamma H$, that are sensitive to the spin and orbital structure of the ordered phase, the strength and orientation of the static NMR field, and the *rf* field ("tipping field") used to excite the nuclear spins. In the high field limit, $\omega_L \gg \Omega$, where $\Omega \sim \Omega_A$ is the dynamical timescale set by the dipole energy, we use Fomin's formulation of the spin dynamics based on the separation of fast and slow timescales for the dynamics of the magnetization (see also Ref. 29), or total spin, $\vec{S}(t)$, and the order parameter, $A(t)$. The "fast" response is on the scale set by the Larmor freqency, $\omega \sim \omega_L$, while the "slow" response is set by the dipolar frequency of order Ω_A.[30] Note that the static NMR field is still assumed to be small in the sense that the Zeeman energy is much smaller than the condensation and gradient energies associated with the orbital components of the order parameter. Thus, the dynamical contributions

to the nuclear dipole and Zeeman energies can be calculated on the basis of the solutions for the orbital order parameter in zero field. However, for static NMR fields greater than the Dipole field, $H \gg H_D \approx 30\,\mathrm{G}$, the equilibrium orientation of the spin components of the order parameter is determined primarily by the Zeeman energy, with the dipole energy resolving any remaining degeneracy in the equilibrium orientation of the $\hat{d}$ vector, or the rotation matrix $\mathbf{R}$ for the $\mathrm{B}_{\mathbf{SO(2)}}$ state. This provides us with the initial equilibrium conditions for orientation of the spin components of the order parameter.

The spin dynamics of the superfluid phases is parametrized in terms of rotation matrices for the precession of the order parameter, e.g. $A(t)$ and total spin, $\vec{S}(t)$, following an initial *rf* excitation of the spin system. An *rf* impulse applied at $t = 0$ rotates ("tips") the total spin, $\vec{S}(t = 0^+)$ by an angle β relative to the equilibrium spin, $\vec{S}_0 || \vec{H} \equiv H\hat{\mathbf{z}}'$. The resulting dynamics of the order parameter for timescales, $0 < t \ll 2\pi/\Omega$, is the parametrized by[30]

$$A(t) = \mathbf{R}_{\mathbf{z}'}(\omega t)\mathbf{R}_{\mathbf{y}'}(\beta)\mathbf{R}_{\mathbf{z}'}(-\omega t + \vartheta)A_0\,, \qquad (29)$$

where $\mathbf{y}' \perp \mathbf{z}'$ is the direction of the *rf* tipping field, and the rotation angles are defined by one "fast" angle, ωt, and two "slow" dynamical angles, β and ϑ. Inserting this expression into Eq. 26 for the dipole energy and averaging the result over the fast time scale, $2\pi/\omega$, gives the fast-time and short-distance scale averaged dipole energy density,

$$\overline{f_D} = \frac{\omega}{2\pi}\int_0^{\frac{2\pi}{\omega}} dt\,\frac{1}{V_{\mathrm{cell}}}\int d^3r\, f_D[A(\vec{r},t)]\,. \qquad (30)$$

This averaged dipolar energy functional determines the transverse NMR frequency shift $\Delta\omega$ as a function of tipping angle β for various orientations of the NMR field, $\vec{H}$, relative to the order parameter within the pore geometry. The variable ϑ – the generalization of Leggett's rotation angle for the bulk B-phase – is fixed by the stationary condition of $\overline{f_D}$. The transverse NMR frequency shift as a function of tipping angle is then given by[30]

$$\omega\Delta\omega = \frac{\gamma^2}{\chi}\frac{1}{\sin\beta}\frac{d}{d\beta}\overline{f_D}\,, \qquad (31)$$

which provides the key NMR signatures for the confined phases of ^{3}He under strong confinement.

B. $\mathbf{P_z}$ and $\mathbf{A_{SO(2)}}$ Phases

The $\mathrm{P}_{\mathbf{z}}$ and $\mathrm{A}_{\mathbf{SO(2)}}$ phases are both ESP phases parameterized by a real $\hat{d}$ vector with order parameters given by Eqs. 20 and 22, respectively. Spatial averaging of the dipole energy for these two phases leads to a dipole energy of the same form for both phases,

$$f_D = g_D\left(2\left\langle\Delta_z^2\right\rangle - \left\langle\Delta_\phi^2\right\rangle\right)\left(\hat{d}\cdot\hat{z}\right)^2\,, \qquad (32)$$

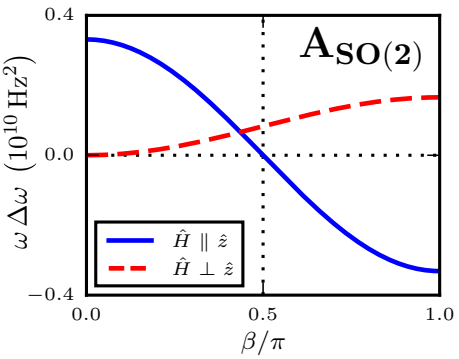

FIG. 12: Frequency shift of the $\mathrm{A}_{\mathbf{SO(2)}}$ phase at $p = 26\,\mathrm{bar}$, $T = 0.5\,T_c$, and $b'_T = 0$. The $\mathrm{P}_{\mathbf{z}}$ phase has the same functional form, but with larger amplitude.

where $\hat{z}$ is the axis of the cylindrical pore, and $\hat{d}$ is homogeneous and oriented in equilibrium in the plane perpendicular to the NMR field $\vec{H}$ and along a direction that minimizes Eq. 32.

Parameterizing the direction of the NMR field in the coordinate system of the cylindrical pore by $\hat{\mathbf{z}}' = \{\cos\phi\sin\theta, \sin\phi\sin\theta, \cos\theta\}$, carrying out the transformation Eq. 29 yields $\overline{f_D}$ in Eq. 30,

$$\overline{f_D} = \frac{1}{8}g_D\left(\left\langle\Delta_\phi^2\right\rangle - 2\left\langle\Delta_z^2\right\rangle\right)\left[2(\cos\beta+1)^2\cos^2\vartheta\sin^2\theta + 4\cos^2\beta - (2\cos\beta + 7\cos^2\beta)\sin^2\theta\right]\,. \qquad (33)$$

Since $\langle\Delta_\phi^2\rangle - 2\langle\Delta_z^2\rangle < 0$ in the pore, $\overline{f_D}$ is minimized with respect to ϑ with $\vartheta = 0$. Finally, a general expression for the transverse shifts as a function of tipping angle is obtained with Eq. 31,

$$\omega\Delta\omega = \frac{\gamma^2}{\chi_N}g_D\left(2\left\langle\Delta_z^2\right\rangle - \left\langle\Delta_\phi^2\right\rangle\right) \times\left[\cos(\beta) - \sin^2(\theta)\left(\frac{5\cos(\beta)-1}{4}\right)\right]\,. \qquad (34)$$

The dependences on the tipping angle, β, and the polar orientation of the NMR field, θ, are identical for both the $\mathrm{P}_{\mathbf{z}}$ and $\mathrm{A}_{\mathbf{SO(2)}}$ phases - only the magnitude of the shift differs between the two phases. Note in particular that the shift vanishes precisely at $\beta = \pi/2$ for $\vec{H}||\hat{z}$. The result for the $\mathrm{A}_{\mathbf{SO(2)}}$ phase is equivalent to what is predicted for a 2D orbital glass phase of ^{3}He-A.[31] Although the $\mathrm{P}_{\mathbf{z}}$ and $\mathrm{A}_{\mathbf{SO(2)}}$ phases differ only quantitatively in their transverse NMR frequency shift, they can still be distinguished in sufficiently clean pores by the change in temperature dependence near the second order phase transition between the two phases (see Fig. 9), in particular the discontinuity in the derivative of the frequency shift, $d\Delta\omega/dT|_{T_{c_2}}$.

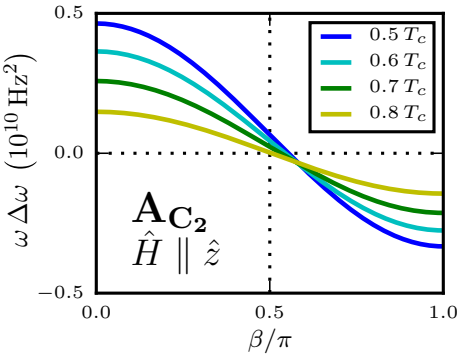

FIG. 13: Transverse frequency shifts for the $\mathrm{A}_{\mathbf{C_2}}$ phase with $\vec{H}\parallel\hat{z}$ at $p=26\,\mathrm{bar}$, temperatures $T=0.5-0.8\,T_c$, and maximal pairbreaking with $b'_T=0$.

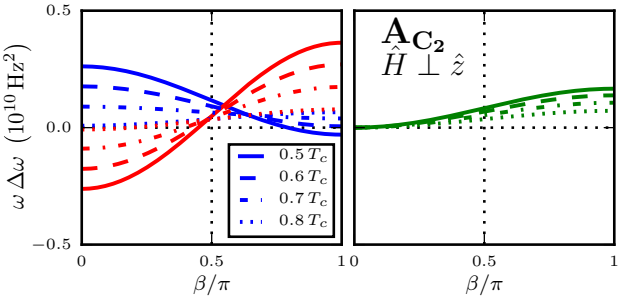

FIG. 14: Transverse frequency shifts for the $\mathrm{A}_{\mathbf{C_2}}$ phase with $\vec{H}\perp\hat{z}$ at $p=26\,\mathrm{bar}$, temperatures $T=0.5-0.8\,T_c$, and maximal pairbreaking with $b'_T=0$. The left panel shows the shifts for in-plane field orientation $\varphi=0$ (blue), and $\varphi=\pi/2$ (red). The right panel shows the shifts for $\varphi=\pi/4$, which has the same functional form as that of the $\mathrm{A}_{\mathbf{SO(2)}}$ phase.

C. $\mathrm{A}_{\mathbf{C_2}}$ Phase

The $\mathrm{A}_{\mathbf{C_2}}$ phase, with order parameter given by Eq. 24, breaks SO(2) orbital symmetry, and exhibits distinctly different NMR signatures compared to those of the $\mathrm{A}_{\mathbf{SO(2)}}$ phase. Here we consider the two cases $\vec{H}\parallel\hat{z}$ and $\vec{H}\perp\hat{z}$. For $\vec{H}\perp\hat{z}$ the residual D_{2h} symmetry leads to a dependence of the transverse frequency shift on the azimuthal angle of $\vec{H}$. Due to the ϕ dependence of the order parameter it is convenient to work in Cartesian coordinates with the chiral axis fixed along $\langle\vec{l}\rangle\parallel\hat{y}$. The resulting spatial averages of the order parameter profiles entering the average dipole energy become,

$$\begin{aligned}\langle\Delta_x^2\rangle &= \langle(\Delta_r\cos\phi-\Delta_\phi\sin\phi)^2\rangle\\ \langle\Delta_y^2\rangle &= \langle(\Delta_r\sin\phi+\Delta_\phi\cos\phi)^2\rangle\\ \langle\Delta_x\Delta_y\rangle &= \langle(\Delta_r\cos\phi-\Delta_\phi\sin\phi)\\ &\quad\times(\Delta_r\sin\phi+\Delta_\phi\cos\phi)\rangle=0\,,\end{aligned}\tag{35}$$

For $\vec{H}\parallel\hat{z}$, the result for the transverse frequency shift for the $\mathrm{A}_{\mathbf{C_2}}$ phase becomes

$$\begin{aligned}\omega\Delta\omega^{(\parallel)} = \frac{1}{2}\frac{\gamma^2}{\chi_N}g_D\,\big\{&\langle\Delta_y^2\rangle-\langle\Delta_x^2\rangle\\ &-\left(3\langle\Delta_x^2\rangle+\langle\Delta_y^2\rangle-4\langle\Delta_z^2\rangle\right)\cos\beta\\ &+2\left|\langle\Delta_y^2\rangle-\langle\Delta_x^2\rangle\right|(1+\cos\beta)\big\}\,.\end{aligned}\tag{36}$$

The results for $\omega\Delta\omega$ for several temperatures are shown in Fig. 13. The shift is similar to that for the $\mathrm{P}_{\mathbf{z}}$ and $\mathrm{A}_{\mathbf{SO(2)}}$ phases, except for the asymmetry of the positive and negative shifts. Note also that $\Delta\omega$ vanishes at a temperature-dependent angle $\beta^*>\pi/2$.

In contrast, for $\vec{H}=H(\cos\varphi\hat{x}+\sin\varphi\hat{y})$ the shift, $\omega\Delta\omega$, depends on the azimuthal angle φ of the static field, in addition to the tipping angle β. For an order parameter of the form in Eq. 24 we have $\langle\vec{l}\rangle\parallel\hat{y}$, and the resulting transverse frequency shift as a function of φ and β becomes,

$$\begin{aligned}\omega\Delta\omega^{(\perp)} = \frac{1}{4}\frac{\gamma^2}{\chi_N}g_D\,\big\{&\left(\langle\Delta_x^2\rangle+\langle\Delta_y^2\rangle-2\langle\Delta_z^2\rangle\right)(\cos\beta-1)\\ &+\left(\langle\Delta_x^2\rangle-\langle\Delta_y^2\rangle\right)(1+7\cos\beta)\cos2\varphi\big\}\,.\end{aligned}\tag{37}$$

The results for several field orientations, $\varphi=0,\pi/4\,,\pi/2$, are shown in Fig. 14. The tipping angle dependences for $\vec{H}\parallel\langle\vec{l}\rangle$ and $\vec{H}\perp\langle\vec{l}\rangle$ are of the same functional form as the corresponding cases for bulk ^{3}He-A. There is a "magic" tipping angle of $\beta_x=\cos^{-1}(-1/7)\approx0.545\pi$ at which $\Delta\omega(\varphi=0)=\Delta\omega(\varphi=\pi/2)$ independent of temperature. The tipping angle dependence for $\varphi=\pi/4$ is much weaker, and qualitatively similar to that for the $\mathrm{A}_{\mathbf{SO(2)}}$ phase with $\vec{H}\perp\hat{z}$. Observation of these results for several field orientations would provide a clear identification of the $\mathrm{A}_{\mathbf{C_2}}$ phase and determine the direction of the mean chiral axis.

D. $\mathrm{B}_{\mathbf{SO(2)}}$ Phase

The $\mathrm{B}_{\mathbf{SO(2)}}$ phase is a non-ESP phase with a reduced and anisotropic spin susceptibility below T_c. The $\mathrm{B}_{\mathbf{SO(2)}}$ phase also exhibits tipping angle dependence of the frequency shift similar to that of ^{3}He-B. In particular, for $\vec{H}\perp\hat{z}$ the shift is a polar-distorted Brinkman-Smith mode, and for $\vec{H}\parallel\hat{z}$ we find the "perpendicular" mode that is qualitatively similar, but with important quantitative differences compared to bulk ^{3}He-B.

For $\vec{H}\parallel\hat{z}$, the Zeeman energy is minimized in equilibrium by a spin-rotation $\mathbf{R}_{\hat{\mathbf{n}}}(\pi/2)$, where $\hat{n}$ is in the $x-y$ plane. This rotation leads to a positive transverse frequency shift that is maximal at small tipping angles, unlike the Brinkman-Smith mode. The quantitative description of the frequency shift depends on the spatial

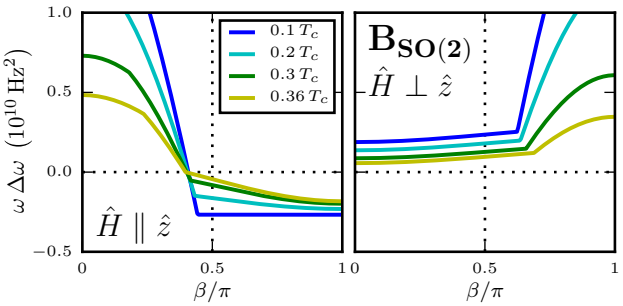

FIG. 15: Transverse frequency shifts for the $\mathrm{B}_{\mathbf{SO(2)}}$ phase at $p = 10\,\mathrm{bar}$, temperatures $T = 0.1\,T_c$, $0.2\,T_c$, $0.3\,T_c$, $0.36\,T_c$, and maximal pair-breaking, $b'_T = 0$.

averages of the $\mathrm{B}_{\mathbf{SO(2)}}$ gap parameters,

$$\begin{aligned} P &= \langle \Delta_r \Delta_z \rangle + \langle \Delta_\phi \Delta_z \rangle \\ Q &= \langle \Delta_r^2 \rangle + 2\,\langle \Delta_r \Delta_\phi \rangle + \langle \Delta_\phi^2 \rangle \\ R &= \langle \Delta_r^2 \rangle + \langle \Delta_\phi^2 \rangle + 4\,\langle \Delta_z^2 \rangle \ , \end{aligned} \tag{38}$$

with the resulting transverse shift for $\vec{H} \parallel \hat{z}$ given by

$$\omega\Delta\omega^{(\parallel)} = \frac{1}{8}\frac{\gamma^2}{\chi_B} g_D \left\{ 4R\,\cos\beta + 4P\,(1+4\cos\beta)\cos\vartheta - Q\,(1+\cos\beta)\cos 2\vartheta \right\} , \tag{39}$$

where the Leggett angle is

$$\cos\vartheta = \begin{cases} +1 & : \beta \le \beta'_L \,, \\ \frac{2P(2\cos\beta - 1)}{Q(1+\cos\beta)} & : \beta'_L < \beta < \beta_L \,, \\ -1 & : \beta \ge \beta_L \,, \end{cases} \tag{40}$$

with $\cos\beta'_L = (2P+Q)/(4P-Q)$ and $\cos\beta_L \equiv (2P-Q)/(4P+Q)$.[32] The left panel of Fig. 15 shows the tipping-angle dependence of the frequency shift $\Delta\omega^{(\parallel)}$ for temperatures starting just below the transition to $\mathrm{B}_{\mathbf{SO(2)}}$-$\mathrm{A}_{\mathbf{C_2}}$ phase boundary at $p = 10\,\mathrm{bar}$. At this pressure transition from the $\mathrm{P}_{\mathbf{z}}$ phase to the $\mathrm{B}_{\mathbf{SO(2)}}$ phase is interrupted by a narrow sliver of $\mathrm{A}_{\mathbf{C_2}}$ phase. Thus, near the $\mathrm{B}_{\mathbf{SO(2)}}$-$\mathrm{A}_{\mathbf{C_2}}$ phase boundary, the $\mathrm{P}_{\mathbf{z}}$ order parameter is dominant and that is reflected in the tipping angle dependence for $T = 0.36T_c$. At lower temperatures the transverse components of the $\mathrm{B}_{\mathbf{SO(2)}}$ become significant and the transverse shift evovles towards a form characteristic of the B-phase with a sharp transition at β_L. The polar distortion is still manifest as the negative shift for $\beta > \beta_L$.

For the static NMR field $\vec{H} \perp \hat{z}$ the relevant averages of the $\mathrm{B}_{\mathbf{SO(2)}}$ gap are

$$\begin{aligned} P &= \langle \Delta_r^2 \rangle + \langle \Delta_\phi^2 \rangle + 2\,\langle \Delta_r \Delta_\phi \rangle + 2\,\langle \Delta_r \Delta_z \rangle + 2\,\langle \Delta_\phi \Delta_z \rangle \\ Q &= 3\,\langle \Delta_r^2 \rangle + 3\,\langle \Delta_\phi^2 \rangle + 2\,\langle \Delta_r \Delta_\phi \rangle \\ &\quad + 8\,\langle \Delta_r \Delta_z \rangle + 8\,\langle \Delta_\phi \Delta_z \rangle + 8\,\langle \Delta_z^2 \rangle \\ R &= 11\,\langle \Delta_r^2 \rangle + 11\,\langle \Delta_\phi^2 \rangle + 18\,\langle \Delta_r \Delta_\phi \rangle + 8\,\langle \Delta_z^2 \rangle \ , \end{aligned} \tag{41}$$

leading to a transverse shift

$$\omega\Delta\omega^{(\perp)} = -\frac{1}{16}\frac{\gamma^2}{\chi_B} g_D \left\{ 2R\,\cos\beta + 4P\,(1+4\cos\beta)\cos\vartheta + Q\,(1+\cos\beta)\cos 2\vartheta \right\} , \tag{42}$$

where

$$\cos\vartheta = \begin{cases} \frac{-2P(2\cos\beta - 1)}{Q(1+\cos\beta)} & : \beta < \beta_L. \\ 1 & : \beta \ge \beta_L. \end{cases} \tag{43}$$

and $\cos\beta_L = (2P-Q)/(4P+Q)$. Unlike bulk ^{3}He-B, the confinement induced anisotropy of the $\mathrm{B}_{\mathbf{SO(2)}}$ order parameter results in a nonzero transverse frequency shift even at small tipping angles, and a temperature dependent critial angle β_L. Once again the frequency shift shows the evolution from a functional form close to the $\mathrm{P}_{\mathbf{z}}$ phase for $T = 0.36T_c$ towards the polar distored B-phase at low temperature.

VI. SUMMARY AND OUTLOOK

For ^{3}He in a long cylindrical pore of radius $R = 100\,\mathrm{nm}$, the relative stability of superfluid phases is strongly dependent on pressure both through the combination of strong-coupling corrections to the fourth-order GL free energy and changes in the effective confinement ratio $R/\xi_0(p)$, and the degree of pairbreaking by boundary scattering. We find four different equilibrium phases over the full pressure range for boundary conditions spanning the range from maximal pairbreaking (retro-reflective boundaries) to minimal pairbreaking (specular reflective boundaries). The first instability is to the z-aligned polar $\mathrm{P}_{\mathbf{z}}$ phase, except for the idealized case of perfect specular reflection for a perfectly circular pore. A polar distorted B-like phase is stabilized at sufficiently low temperatures within our theory for the strong-coupling effects based on the GL functional. We find two symmetry inequivalent chiral A-like phases, the axially symmetric $\mathrm{A}_{\mathbf{SO(2)}}$ phase with a radially directed chiral field and a polar core favored in the limit of weak pairbreaking, and the broken axial symmetry chiral $\mathrm{A}_{\mathbf{C_2}}$ phase with chirality directed perpendicular to the axis of the pore. The $\mathrm{A}_{\mathbf{SO(2)}}$ phase dominates the phase diagram for specularly reflecting boundaries while the $\mathrm{A}_{\mathbf{C_2}}$ phase appears at intermediate temperatures and higher pressures separating the $\mathrm{P}_{\mathbf{z}}$ and $\mathrm{B}_{\mathbf{SO(2)}}$ phases. The four equilibrium phases can be identified by their distinct NMR freqency shifts as functions of tipping angle and NMR field orientation. NMR experiments utilizing arrays of equivalent nano-pores should be able to test these predictions and uniquely identify the polar phase as well as the new prediction of the broken symmetry chiral $\mathrm{A}_{\mathbf{C_2}}$ phase.

The interplay of complex symmetry breaking, spatial confinement, surface disorder and strong-interactions beyond weak-coupling BCS leads to a remarkably rich phase diagram of broken symmetry states in what is perhaps the simplest of confining geometries, the cylindrical pore.

We expect an even wider spectrum of broken symmetry phases with unique physical properties in more complex confining geometries,[34] or when confinement is in competition with external fields or the formation of topological defects.[35,36] Indeed theoretical reports of new phases of superfluid ^{3}He in thin films and cavities have simulated the development of nano-scale cavities, MEMS and nanofluidic oscillators and new nano-scale materials for experimental search and discovery of new quantum ground states. In the latter category the infusion of quantum fluids into highly porous anisotropic aerogels has opened a new window into the role of confinement on complex symmetry breaking. New chiral and ESP phases of superfluid ^{3}He in uniaxially stretched and compressed silica aerogels have been reported,[3,37,38] and in a new class of nano-scale confining media, called "nematic" aerogels, there is strong evidence to support the observation of a polar $\mathrm{P}_{\mathbf{z}}$ phase of ^{3}He in this strongly anisotropic *random* medium.[4,39] From the vantage point of our predictions for ^{3}He confined in a long cylindrical pore there are strong similarities between the phase diagram for $R = 100\,\mathrm{nm}$ cylindrical pores and the experimental phase diagram of ^{3}He in nematic aerogels, including the normal to $\mathrm{P}_{\mathbf{z}}$ transition, and uniaxially deformed B-like and chiral A-like phases. It is remarkable that the subtle correlations giving rise to chirality of an $\mathrm{A}_{\mathbf{C_2}}$ or $\mathrm{A}_{\mathbf{SO(2)}}$ phase survives the random potential of these disordered porous solids. The observations pose challenges for theorists to provide a quantitative understanding of how complex symmetry breaking and long-range order remain so robust in random anisotropic materials.

VII. MATERIAL PARAMETERS

The following tables summarize the pressure dependent material parameters that determine the superfluid phases in strong-coupling GL theory.

p[bar]	T_c[mK]	v_f[m/s]	ξ_0[nm]	$\Delta\beta_1^{\rm sc}$	$\Delta\beta_2^{\rm sc}$	$\Delta\beta_3^{\rm sc}$	$\Delta\beta_4^{\rm sc}$	$\Delta\beta_5^{\rm sc}$
0.0	0.929	59.03	77.21	0.03	-0.11	0.10	-0.15	0.16
2.0	1.181	55.41	57.04	0.03	-0.04	-0.14	-0.37	0.19
4.0	1.388	52.36	45.85	0.02	-0.01	-0.24	-0.48	0.19
6.0	1.560	49.77	38.77	0.02	-0.01	-0.28	-0.54	0.18
8.0	1.705	47.56	33.91	0.02	-0.02	-0.30	-0.58	0.17
10.0	1.828	45.66	30.37	0.01	-0.03	-0.31	-0.60	0.15
12.0	1.934	44.00	27.66	0.01	-0.04	-0.31	-0.61	0.13
14.0	2.026	42.51	25.51	0.00	-0.05	-0.30	-0.62	0.11
16.0	2.106	41.17	23.76	0.00	-0.05	-0.27	-0.66	0.10
18.0	2.177	39.92	22.29	0.00	-0.06	-0.27	-0.68	0.09
20.0	2.239	38.74	21.03	-0.01	-0.06	-0.26	-0.69	0.07
22.0	2.293	37.61	19.94	-0.01	-0.07	-0.26	-0.71	0.06
24.0	2.339	36.53	18.99	-0.01	-0.07	-0.26	-0.72	0.04
26.0	2.378	35.50	18.15	-0.02	-0.07	-0.27	-0.73	0.03
28.0	2.411	34.53	17.41	-0.02	-0.07	-0.27	-0.74	0.01
30.0	2.438	33.63	16.77	-0.02	-0.07	-0.28	-0.74	-0.01
32.0	2.463	32.85	16.22	-0.03	-0.07	-0.27	-0.75	-0.02
34.0	2.486	32.23	15.76	-0.03	-0.07	-0.27	-0.75	-0.03

TABLE I: Material parameters for ^{3}He vs. pressure, with T_c from Ref. 25, v_f calculated with m^* from Ref. 25 and density n from Ref. 26. Coherence lengths are calculated as $\xi_0 = \hbar v_f/2\pi\, k_B T_c$. Strong-coupling $\Delta\beta_i^{\rm sc}$ parameters at T_c in units of $|\beta_1^{\rm wc}|$ are from Ref. 24.

n	$\Delta\beta_1^{\rm sc}$	$\Delta\beta_2^{\rm sc}$	$\Delta\beta_3^{\rm sc}$	$\Delta\beta_4^{\rm sc}$	$\Delta\beta_5^{\rm sc}$
0	$3.070{\times}10^{-2}$	$-1.074{\times}10^{-1}$	$1.038{\times}10^{-1}$	$-1.593{\times}10^{-1}$	$1.610{\times}10^{-1}$
1	$-2.081{\times}10^{-3}$	$5.412{\times}10^{-2}$	$-1.752{\times}10^{-1}$	$-1.350{\times}10^{-1}$	$2.263{\times}10^{-2}$
2	$2.133{\times}10^{-5}$	$-1.081{\times}10^{-2}$	$3.488{\times}10^{-2}$	$1.815{\times}10^{-2}$	$-4.921{\times}10^{-3}$
3	$-4.189{\times}10^{-7}$	$1.025{\times}10^{-3}$	$-4.243{\times}10^{-3}$	$-1.339{\times}10^{-3}$	$3.810{\times}10^{-4}$
4	—	$-5.526{\times}10^{-5}$	$3.316{\times}10^{-4}$	$5.316{\times}10^{-5}$	$-1.529{\times}10^{-5}$
5	—	$1.722{\times}10^{-6}$	$-1.623{\times}10^{-5}$	$-1.073{\times}10^{-6}$	$3.071{\times}10^{-7}$
6	—	$-2.876{\times}10^{-8}$	$4.755{\times}10^{-7}$	$8.636{\times}10^{-9}$	$-2.438{\times}10^{-9}$
7	—	$1.991{\times}10^{-10}$	$-7.587{\times}10^{-9}$	—	—
8	—	—	$5.063{\times}10^{-11}$	—	—

TABLE II: Coefficients of a polynomial fit to the strong-coupling β parameters from Ref. 24 of the form $\Delta\beta_i^{\rm sc} = \sum_n a_n^{(i)}\, p^n$.

p[bar]	$\Delta\beta_1^{\rm sc}$	$\Delta\beta_2^{\rm sc}$	$\Delta\beta_3^{\rm sc}$	$\Delta\beta_4^{\rm sc}$	$\Delta\beta_5^{\rm sc}$
0	-0.008	-0.033	-0.043	-0.054	-0.055
12	-0.034	-0.080	-0.117	-0.199	-0.194
16	-0.041	-0.088	-0.129	-0.230	-0.236
20	-0.048	-0.095	-0.136	-0.254	-0.277
24	-0.055	-0.101	-0.140	-0.272	-0.320
26	-0.059	-0.103	-0.140	-0.280	-0.344
28	-0.062	-0.105	-0.139	-0.287	-0.370
30	-0.066	-0.106	-0.137	-0.292	-0.398
32	-0.070	-0.106	-0.132	-0.296	-0.429
34.4	-0.074	-0.103	-0.123	-0.298	-0.469

TABLE III: Sauls-Serene $\Delta\beta_i^{\rm sc}$ parameters[23] for ^{3}He vs. pressure. The values at $p = 0\,\mathrm{bar}$ were obtained by extrapolating the published $\Delta\beta_i^{\rm sc}$, which were calculated only down to 12 bar, to their weak-coupling values at $\lim_{p\to p_0} T_c(p)/T_F(p) = 0$, which corresponds to a negative pressure of $p_0 = -5\,\mathrm{bar}$.

n	$\Delta\beta_1^{\rm sc}$	$\Delta\beta_2^{\rm sc}$	$\Delta\beta_3^{\rm sc}$	$\Delta\beta_4^{\rm sc}$	$\Delta\beta_5^{\rm sc}$
0	$-8.311{\times}10^{-3}$	$-3.334{\times}10^{-2}$	$-4.298{\times}10^{-2}$	$-5.416{\times}10^{-2}$	$-5.505{\times}10^{-2}$
1	$-2.404{\times}10^{-3}$	$-4.716{\times}10^{-3}$	$-7.988{\times}10^{-3}$	$-1.550{\times}10^{-2}$	$-1.427{\times}10^{-2}$
2	$2.813{\times}10^{-5}$	$8.032{\times}10^{-5}$	$1.637{\times}10^{-4}$	$3.174{\times}10^{-4}$	$2.942{\times}10^{-4}$
3	$-4.024{\times}10^{-7}$	$-9.400{\times}10^{-8}$	$-1.345{\times}10^{-8}$	$-2.138{\times}10^{-6}$	$-6.654{\times}10^{-6}$

TABLE IV: Coefficients of a polynomial fit to the Sauls-Serene β parameters in Table III of the form $\Delta\beta_i^{\rm sc} = \sum_n a_n^{(i)}\, p^n$.

VIII. ACKNOWLEDGEMENTS

The research of JJW and JAS was supported by the National Science Foundation (Grant DMR-1106315). We acknowledge key discussions with Erkki Thuneberg and Anton Vorontsov on boundary conditions for the GL theory of ^{3}He in confined geometries, and with Bill Halperin and Andrew Zimmerman on experimental realizations of superfluidity with strong confinement that provided important motivation for this study.

[1] V. Ambegaokar, P. G. de Gennes, and D. Rainer. Landau-ginzburg equations for an anisotropic superfluid. *Phys. Rev. A*, 9:2676, 1975.

[2] L. V. Levitin, R. G. Bennett, A. Casey, B. Cowan, J. Saunders, D. Drung, Th. Schurig, and J. M. Parpia. Phase Diagram of the Topological Superfluid ^{3}He Confined in a Nanoscale Slab Geometry. *Science*, 340(6134):841–844, 2013.

[3] J. Pollanen, J. I. A. Li, C. A. Collett, W. J. Gannon, W. P. Halperin, and J. A. Sauls. New chiral phases of superfluid ^{3}He stabilized by anisotropic silica aerogel. *Nature Physics*, 8(4): 317–320, 2012.

[4] R. Sh. Askhadullin, V. V. Dmitriev, D. A. Krasnikhin, P. N. Martynov, A. A. Osipov, A. A. Senin, and A. N. Yudin. Phase diagram of superfluid ^{3}He in nematically ordered aerogel. *JETP Lett.*, 95(6):326–331, 2012.

[5] S. B. Chung and S.-C. Zhang. Detecting the Majorana Fermion Surface State of ^{3}He-B through Spin Relaxation. *Phys. Rev. Lett.*, 103(23):235301, 2009.

[6] R. Nomura, S. Murakawa, M. Wasai, K. Akiyama, T. Nakao, and Y. Okuda. Surface Majorana cone of the topological superfluid ^{3}He-B phase. *Physica E*, 55:42–47, 2014.

[7] T. Mizushima and K. Machida. Effects of Majorana Edge Fermions on Dynamical Spin Susceptibility in Topological Superfluid ^{3}He-B. *J. Low Temp. Phys.*, 162(3-4):204–211, 2011.

[8] T. Mizushima. Superfluid ^{3}He in a restricted geometry with a perpendicular magnetic field. *Phys. Rev. B*, 86(9):094518, 2012.

[9] H. Wu and J. A. Sauls. Majorana excitations, spin and mass currents on the surface of topological superfluid ^{3}He-B. *Phys. Rev. B*, 88(18):184506, 2013.

[10] K. Maki. Planar textures in superfluid ^{3}He-A. *J. Low Temp. Phys.*, 32(1-2):1–17, 1978.

[11] A. L. Fetter and S. Ullah. Superfluid density and critical current of ^{3}He in confined geometries. *J. Low Temp. Phys.*, 70(5-6): 515–535, 1988.

[12] T. Takagi. AB Phase Transition of Superfluid ^{3}He Confined in Pore Geometry. *Prog. Theor. Phys.*, 78(3):562–572, 1987.

[13] Y.-H. Li and T.-L. Ho. Superfluid ^{3}He in very confined regular geometries. *Phys. Rev. B*, 38(4):2362, 1988.

[14] C. M. Gould and D. M. Lee. Superfluid ^{3}He in Narrow Cylinders. *Phys. Rev. Lett.*, 41(14):967, 1978.

[15] J. Saunders, D. S. Betts, D. F. Brewer, S. J. Swithenby, and W. S. Truscott. Observations on Superfluid ^{3}He-A in Small Cylinders: Evidence for a Textural Transition. *Phys. Rev. Lett.*, 40(19):1278, 1978.

[16] R. Bruinsma and K. Maki. Textures in narrow cylinders in superfluid ^{3}He-A. *J. Low Temp. Phys.*, 37(5-6):607–625, 1979.

[17] H. Masuda and K. Fukuda. Ordered metal nanohole arrays made by a two-step replication of honeycomb structures of anodic alumina. *Science*, 268(5216):1466–1468, 1995.

[18] M. Gonzalez, P. Zheng, E. Garcell, Y. Lee, and H. B. Chan. Comb-drive micro-electro-mechanical systems oscillators for low temperature experiments. *Review of Scientific Instruments*, 84 (2):025003, 2013.

[19] N. Zhelev, R. G. Bennett, E. N. Smith, J. Pollanen, W. P. Halperin, and J. M. Parpia. Dissipation signatures of the normal and superfluid phases in torsion pendulum experiments with ^{3}He in aerogel. *Phys. Rev. B*, 89(9):094513, 2014.

[20] X. Rojas and J. P. Davis. Superfluid nanomechanical resonator for quantum nanofluidics. *Phys. Rev. B*, 91(2):024503, 2015.

[21] L. J. Buchholtz and A. L. Fetter. Textures in superfluid ^{3}He-A: Hydrodynamic and magnetic effects in a cylindrical pore. *Phys. Rev. B*, 15(11):5225, 1977.

[22] D. Rainer and J. W. Serene. Free energy of superfluid ^{3}He. *Phys. Rev. B*, 13(11):4745, 1976.

[23] J. A. Sauls and J. W. Serene. Potential Scattering Models for the Quasiparticle Interactions in Liquid ^{3}He. *Phys. Rev.*, B24: 183, 1981.

[24] H. Choi, J. P. Davis, J. Pollanen, T. M. Haard, and W. P. Halperin. Strong coupling corrections to the Ginzburg-Landau theory of superfluid ^{3}He. *Phys. Rev. B*, 75(17):174503, 2007.

[25] D. S. Greywall. ^{3}He specific heat and thermometry at millikelvin temperatures. *Phys. Rev. B*, 33(11):7520, 1986.

[26] J. C. Wheatley. Experimental properties of superfluid ^{3}He. *Rev. Mod. Phys.*, 47(2):415, 1975.

[27] J. A. Sauls. Surface states, Edge Currents, and the Angular Momentum of Chiral p-wave Superfluids. *Phys. Rev. B*, 84: 214509, 2011.

[28] Recently Aoyama has shown that a translational symmetry breaking "stripe" B-like phase along the axis of the channel may be possible in cylindrical geometries, stabilized with an anisotropic boundary condition that implements specular reflection for scattering along z, but retro-reflection in the r-ϕ plane. This enhances $A_{\alpha z}$ on the boundary relative to $A_{\alpha\phi}$.[33] Our boundary condition has the opposite anisotropy. Thus, with our formulation it is unclear if conditions allow for an energetically stable B-like stripe phase. This question will be addressed in a separate report.

[29] Yu. M. Bunkov and G. E. Volovik. On the Possibility of the Homogeneously Precessing Domain in Bulk ^{3}He-A. *Eur. Phys. Lett.*, 21(8):837–844, 1993.

[30] I. A. Fomin. Solution of spin dynamics equations for ^{3}He superfluid phases in a strong magnetic field. *J. Low Temp. Phys.*, 31(3-4):509–526, 1978.

[31] V. V. Dmitriev, D. A. Krasnikhin, N. Mulders, A. A. Senin, G. E. Volovik, and A. N. Yudin. Orbital glass and spin glass states of ^{3}He-A in aerogel. *Sov. Phys. JETP Lett.*, 91(11):599–606, 2010.

[32] Note that χ_B entering both Eqs. 39 and 42 is given by $\chi_B = \chi_N/[1 + g_z/\chi_N(\langle\Delta_r^2\rangle + \langle\Delta_\phi^2\rangle)] < \chi_N$. This result is obtained in both cases by minimizing the Zeeman energy for the specific field orientation.

[33] K. Aoyama. Stripe order in superfluid ^{3}He confined in narrow cylinders. *Phys. Rev. B*, 89(14):140502, 2014.

[34] J. J. Wiman and J. A. Sauls. Superfluid phases of ^{3}He in a periodic confined geometry. *J. Low Temp. Phys.*, 174:1–14, 2013.

[35] A. B. Vorontsov and J. A. Sauls. Domain Walls in Superfluid ^{3}He-B. *J. Low Temp. Phys.*, 138:283–288, 2005.

[36] A. B. Vorontsov and J. A. Sauls. Crystalline Order in Superfluid ^{3}He Films. *Phys. Rev. Lett.*, 98(4):045301, 2007.

[37] R. Bennett, N. Zhelev, E. Smith, J. Pollanen, W. Halperin, and J. Parpia. Modification of the ^{3}He Phase Diagram by Anisotropic Disorder. *Phys. Rev. Lett.*, 107:235504, 2011.

[38] J. A. Sauls. Chiral phases of superfluid ^{3}He in an anisotropic medium. *Phys. Rev. B*, 88:214503, 2013.

[39] V. V. Dmitriev, A. A. Senin, A. A. Soldatov, and A. N. Yudin. Polar phase of superfluid ^{3}He in anisotropic aerogel. *arXiv*, 1507.04275:1–5, 2015.